Image-driven Simulation of Brain Tumors Using a Reaction-diffusion Mathematical Model

Kristos Qiqi

Supervisors: Lukáš Malý, George Baravdish
Examiner: Neda Haj-Hosseini

LI.U LINKÖPING
UNIVERSITY

Abstract

Brain tumors pose a big challenge in the field of neuro-oncology. Gliomas are the largest subgroup. Magnetic resonance imaging is a non-invasive tool for detecting and characterizing these tumors. Mathematical models, such as the reaction-diffusion equation, can be used for understanding the intricate behavior of gliomas. This thesis aims to improve the understanding and prediction of tumor growth by modifying and evaluating a reaction-diffusion mathematical model and incorporating magnetic resonance (MR) images, namely intensity from T_1-weighted and T_2-weighted images, and apparent diffusion coefficient values.

Image data from five patients was used. The finite difference method was used to approximate the solution, and brain segmentation is performed using the software package FSL. The Jaccard index is used to compare the simulation results with the ground truth, being the segmented tumor area. A spatially varying proliferation rate is introduced and histology images are used to construct an initial condition for the reaction-diffusion mathematical model.

The results show improvement in performance based on the Jaccard index, with the highest values achieved when using a diffusion matrix given as an affine function of intensity in T_1-weighted images. Incorporating a spatially varying proliferation rate reduces the number of iterations required to reach the maximum Jaccard index compared to a constant proliferation rate, but this does not influence the simulation time. The introduction of the p-Laplace operator, particularly with a value of $p = 1.8$ instead of the usual Laplace operator (where $p = 2$), leads to a higher Jaccard index, indicating an improvement in the model's performance. The best Jaccard index achieved was 0.4909 with $p = 1.8$ compared to the basic model (JI $= 0.4382$ with $p = 2$). An initial tumor cell density is constructed using histology images.

In conclusion, insights are provided into improving tumor growth modeling by incorporating MR images, the p-Laplace operator, a spatially varying proliferation rate and possibility of constructing the initial conditions for tumor cell density based on histology images.

Contents

List of Figures

Chapter 1

Introduction

This chapter introduces the biological mechanisms behind tumor growth and progression, more specifically gliomas. The fundamentals of magnetic resonance imaging (MRI) are introduced as well as the modalities used in this thesis. A brief introduction to mathematical modelling for brain tumors using a reaction-diffusion equation is given.

1.1 The Biology of Brain Tumors

The cell is the fundamental building block of life in organisms and it is responsible for many of the functions necessary for survival. Cells replicate and divide into two or more daughter cells, each containing a complete copy of the parent cell's chromosomes. Throughout this process, the cell is prone to mutations, which can alter their normal behavior. One example of abnormal behavior due to mutations is uncontrolled cell division. This can result in the formation of a mass of cells known as tumor. Tumors can either be benign or malignant. Benign tumors are non-cancerous growths and do not spread to other parts of the body. Malignant tumors are cancerous growths and can spread to other parts of the body. This process is called metastasis [25]. In this thesis, we are interested in tumors arising in the brain, more specifically gliomas. This type of tumor arises from the glial cells in the brain which includes astrocytes, oligodendrocytes and ependymal cells, is classified based on the type of glial cell they arise from [26].

Gliomas are graded based on their malignancy. The main groups of gliomas are high-grade gliomas and low-grade gliomas. Low-grade gliomas, usually classified as grade I or grade II tumors, grow slowly and are less aggressive. High grade gliomas grow more rapidly and are more aggressive, usually classified as grade III or grade IV tumors [26].

1.2 Medical Imaging

Medical imaging techniques are used to create visual representations of the interior of a body for clinical analysis and medical intervention. It is a crucial aspect of modern medicine, allowing doctors to diagnose, monitor, and treat diseases effectively.

One of the most commonly used medical imaging methods is MRI. It produces detailed images of the interior of the body using radio waves and a strong magnetic field. MRI uses non-ionizing radiation, in contrast to X-rays and computer tomograph (CT) scans. Instead, it generates signals from body atoms using radio waves and a powerful magnet. It's a non-invasive procedure and is generally safe for most patients and the images produced by these signals can then be interpreted by radiologists [9].

The foundation of MRI is based on the fact that hydrogen ions (protons) in the body can act as magnets due to their spin property, which can be thought of as an intrinsic angular momentum, where there is no motion in space. The protons are charged and have a spin which generates a magnetic field. As a result, the body's protons can be influenced by external magnetic fields, meaning, one can align the spin direction of the protons with an external magnetic field. This can result in a net magnetization from the protons in the body, in the same direction as the external magnetic field. In addition, the external magnetic field generates a torque on the protons, causing them to precess at the so called Larmor frequency [9]. A more detailed description is given in Chapter 2.

In MRI, tumors are typically identified as distinct, abnormal formations that stand out from the surrounding tissue. When it comes to brain tumors in particular, their type and stage might affect how they appear. Depending on the imaging sequence employed, brain tumors typically manifest on the MRI as regions of high or low intensity. They often appear as irregular and asymmetrical masses that contrast with the surrounding healthy brain tissue. After the administration of a contrast agent, some brain tumors may also exhibit enhancement (look brighter on the images), which aids in defining the tumor's boundaries.

1.3 Mathematical Modeling

Mathematical models, particularly those involving partial differential equations (PDEs), can be very useful in modeling tumor progression. One common approach is to use a reaction-diffusion equation, which describes how the concentration of one or more substances changes as a result of local reactions (chemical reactions, growth, and decay) and diffusion (spreading out as a result of random motion). In the context of tumor growth, the substance whose concentration we are interested in could be the cell density of tumor cells. The reaction term then represents the rate at which tumor cells proliferate (for example, through cell division), and the diffusion term represents the spread of tumor cells through tissue [17].

Mathematically, a simple reaction-diffusion equation is given by

$$\frac{\partial u(x,t)}{\partial t} = D\Delta u(x,t) + f(u(x,t)), \tag{1.1}$$

where $u(x,t)$ is the tumor cell density, Δ is the Laplace operator, D is the diffusion coefficient, and $f(u(x,t))$ represents the reaction term usually of the form $f(u) = \rho u(1-u)$, where $\rho > 0$ is the proliferation rate. This reaction term could take many forms, depending on how one wants the tumor growth to be modeled. In general, the diffusion matrix is expected to depend on position in space, then (1.1) becomes

$$\frac{\partial u(x,t)}{\partial t} = \nabla \cdot (D(x)\nabla u(x,t)) + f(u(x,t)), \tag{1.2}$$

where $D(x)$ is the diffusion matrix. To be able to solve (1.2) in a given domain Ω, it is necessary to provide an initial condition $u(x,0) = \phi(x)$ and a boundary condition on the surface S of Ω. There are mainly three types of boundary conditions: Dirichlet boundary conditions, which specify the value of the solution at the boundary, Neumann boundary conditions which specify the normal derivative of the solution at the boundary, and Robin boundary conditions, which is a combination of Dirichlet and Neumann boundary conditions. In this thesis, the focus will be on Neumann boundary conditions. The Neumann boundary condition is then of the form

$$D(x)\nabla u(x,t) \cdot n(x) = 0 \quad \text{for } x \in S,$$

where $n(x)$ is the normal vector to the surface S. In a physical context, the derivative of a quantity often represents a rate of change or a flux. For the reaction-diffusion equation modeling tumor growth, the Neumann boundary condition represents the flux of the cell density at the boundary of the domain, which is assumed to be 0.

1.4 Aim

The aim of this thesis is to enhance the understanding and prediction of tumor growth by modifying and evaluating the reaction-diffusion model based on medical images. This includes the intensity from T_1-weighted and T_2-weighted images, and apparent diffusion coefficient (ADC) values, as well as histology images. This study will also look into the effect of the p-Laplace operator (3.17) on the simulation results. The ultimate goal is to provide a more realistic and accurate representation of tumor growth, which could potentially contribute to better diagnostic and therapeutic strategies.

1.5   Research Questions

The research questions of this thesis are as below:

1. How to improve a reaction-diffusion model by optimizing its parameters.

2. Is it possible to extract tumor cell density from patient images?

3. How can properties of various MR sequences be incorporated into the model?

4. How can the simulations be evaluated? Is the tumor growth realistic?

1.6   Related Work

Mathematical modeling of brain tumor growth, with a particular focus on reaction-diffusion models, has seen extensive research interest in recent years. The application of reaction-diffusion models has been invaluable in providing deeper insights into the growth patterns of brain tumors, aiding in the development of personalized treatment strategies. In this section, several key studies that have significantly contributed to this growing field and are closely related to the subject of this thesis will be discussed.

The authors in [22], incorporate spatial heterogeneity of the diffusion by assuming differing rates of diffusion in white matter and gray matter and use a reaction-diffusion equation to model the cell density of the tumor. Although the precise ratio between the diffusion coefficient in white matter and gray matter can vary across different models, they specifically assumed a 5-fold difference in diffusion rates. They created a precise map of the white and gray matter inside a synthetic brain used for MR simulations. By doing so, they could visualize and study the distinct growth patterns that emerged due to the difference in diffusion rates in the brain.

Further advancements were made in [11] by including anisotropic extension of gliomas. This modification was based on the observation that glial cells have a preference to migrate along the direction of fiber tracts. Their simulations outcomes were compared with two clinical cases demonstrating that the shape and kinetic evolution of low-grade gliomas centered around the insula were better simulated with anisotropic rather than isotropic diffusion. This indicates that it may be necessary to take into account the anisotropy of the cell diffusion tensor while simulating the growth and invasion of gliomas. In order to identify the main white matter tracts in the brain, the study described in [21] established a mathematical model based on diffusion tensor imaging. The anisotropic model offered a marginal advantage over other reaction-diffusion models, but merely for tumors with strong anisotropy.

A parameter estimate approach for reaction-diffusion tumor growth models using medical images captured at different time points was proposed in [13]. This method calculates the model's patient-specific parameters, offering a means of

adjusting the general model to specific patient data. Their findings show that when one parameter, the proliferation rate of tumor cells, was fixed, several more factors could be uniquely identified.

Chapter 2

Magnetic Resonance Imaging

This chapter provides a more technical view of MRI, focusing on the key concepts of T_1 and T_2 relaxation times. These fundamental properties are very important in differentiating tissue types in MRI, thus forming the basis for image contrast.

In addition, this chapter explains MRI modalities that are used in this thesis, such as T_1-weighted, T_2-weighted, and diffusion tensor imaging (DTI). These modalities, offer diverse perspectives on tissue properties. This chapter aims to provide a basic foundation for understanding the technical side of MRI and its application in medical imaging.

2.1 Relaxation Times

2.1.1 T_1-relaxation Time

During an MRI scan, magnetic field is generated, referred to as B_0, by the magnet. This magnetic field aligns the nuclear spins of the atoms within the body, resulting in the creation of a net magnetization.

Net magnetization is a vector quantity that describes the collective alignment of nuclear spins. It is typically represented by three components: M_x, M_y, and M_z. The M_z component corresponds to the magnetization aligned with the direction of the static magnetic field B_0, while M_x and M_y represent the magnetization in the perpendicular directions. The net magnetization is said to be in a state of equilibrium when it is aligned with the external magnetic field, B_0. However, it is possible to disrupt this equilibrium state by altering M_z such that it reaches zero, resulting in the absence of net magnetization in that direction. This can be done by applying a radiofrequency (RF) pulse. The return of M_z to its equilibrium state is governed by the spin lattice relaxation time (T_1). Different tissues in the body exhibit different T_1 values, which are dependent on both the magnitude of B_0 and the specific tissue type. For a more detailed description of the RF pulse and the physics behind, please see [9].

2.1.2 T_2-relaxation Time

The transverse magnetization is usually denoted by M_x and M_y. These magnetic moments are disturbed from their equilibrium state when the RF pulse is applied and then turned off. As time goes on, this leads to phase incoherence in the transverse plane and the eventual decay of M_x and M_y to 0. The process of decay is governed by the spin-spin relaxation time (T_2), which measures the time it takes for the transverse magnetization to decrease exponentially. The value of T_2 varies among different tissues, and is influenced by both the magnitude of the applied magnetic field (B_0) and the tissue type. It is important to note that T_2 is always shorter than the spin lattice relaxation time (T_1). For a detailed description please see [9].

2.2 MRI Modalities

To acquire an MR image, a pulse sequence is applied and it needs to be repeated several times to acquire the desired images. The time between these repetitions (the time from one RF pulse to the next) is called repetition time (TR). This determines the amount of M_z recovered each sequence.

Another important time is echo time (TE). It is the time between the applied RF-pulse and the detection of the signal from the tissue of interest. The amount of the transverse magnetization for each MRI sequence is controlled by TE. Depending on how TR and TE are chosen, different contrasts of MR images are generated. For a detailed description on image acquisition, please see [9].

2.2.1 Structural MRI

T_1-weighted (T_1-w) Images

A T_1-w image shows variations in T1 relaxation times. This is achieved by utilizing a short TE and a short repetition TR during the image acquisition process, which provides distinct contrasts between different tissues. In this modality, cerebrospinal fluid (CSF) appears darker compared to other tissues, as it has a short T1 relaxation time. Fat appears brighter in the image due to its longer T1 relaxation time. White matter appears bright, while gray matter appears as a shade of gray in the T1-w image [19], see Figure 2.1a.

T_2-weighted (T_2-w) Images

A T_2-w image highlights the differences in T_2 relaxation times between different tissues. Both TE and TR are long for T_2-w images. In a T_2-w image, CSF appears bright due to its long T2 relaxation time, white matter exhibits a slightly bright signal, while gray matter, appears darker than white matter[19], see Figure 2.1b.
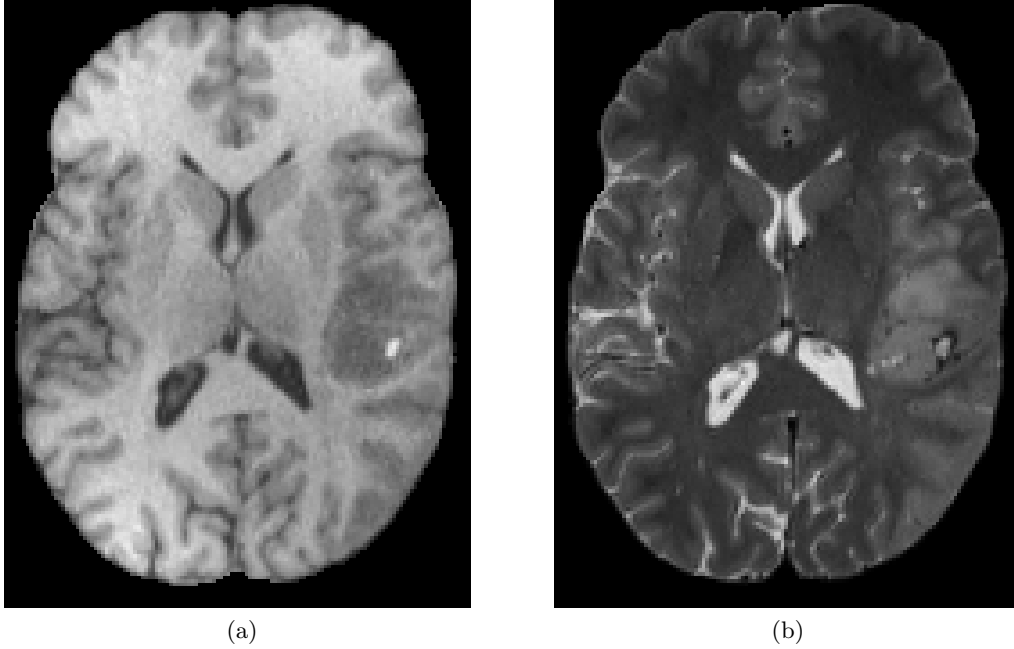
Figure 2.1: (a) T_1-w and (b) T_2-w images of a patient from the UPenn-GBM dataset [1].

2.2.2 Diffusion Weighted Imaging

Diffusion weighted imaging (DWI) utilizes a magnetic field gradient during image acquisition to highlight the areas where water diffusion takes place. Multiple DWI scans are acquired from different directions to build a diffusion tensor image (DTI), allowing the assessment of diffusion in three dimensions. The structure of the brain tissue influences water diffusion in the brain. For example, in dense tissue, such as the axons of neurons, water diffusion is constrained and tends to occur along the length of the axons. This is referred to as anisotropic diffusion. Diffusion of water is more random in locations where the tissue is less dense, and this is referred to as isotropic diffusion. DTI is a group of methods that generates the images of diffusion properties of tissue based on the eigenvalues calculated from DWI. The process of how to acquire DTI images is beyond the scope of this thesis, more details can be be found in [14].

For acquiring a DTI, a tensor is obtained, usually denoted as D, a mathematical object that takes the concept of vectors and matrices and expands it to higher dimensions. This tensor contains information regarding the diffusion direction within each voxel. It can be used to compute several measurements that provide information about the tissue. The main measurements are fractional anisotropy (FA), which quantifies the spread of eigenvalues, and mean diffusivity (MD), which shows the average of all three eigenvalues. Additionally, radial diffusivity (RD),

which is the average of the two smaller eigenvalues, represents diffusion in directions perpendicular to the third direction, and axial diffusivity (AD), quantifies the value of the primary eigenvalue, or the direction of highest diffusion [14]. Figure 2.2 shows brain images for MD (also called ADC), AD and FA from the UPenn-GBM dataset [1, 2, 5].
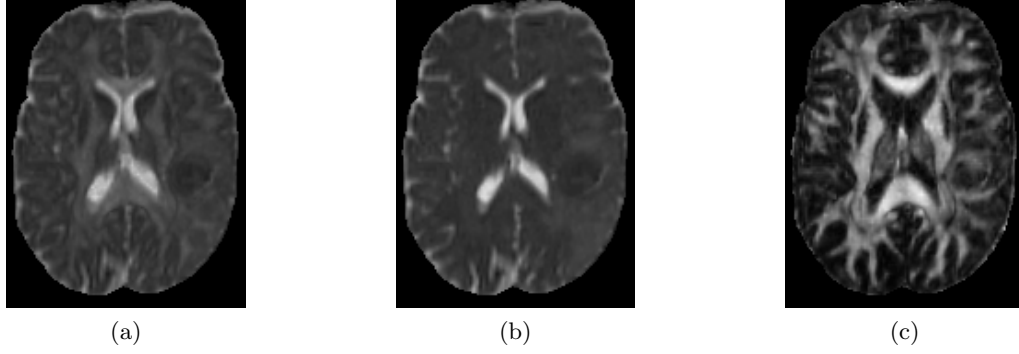
Figure 2.2: (a) *ADC* image, (b) AD image, (c) FA image [1].

Assuming D has eigenvalues λ_1, λ_2, and λ_3 such that $\lambda_1 \leq \lambda_2 \leq \lambda_3$, the measurements described above can be calculated as

$$MD = \frac{\lambda_1 + \lambda_2 + \lambda_3}{3}, \quad RD = \frac{\lambda_1 + \lambda_2}{2}, \quad AD = |D| = \lambda_3$$

$$FA = \sqrt{\frac{3[(\lambda_1 - MD)^2 + (\lambda_2 - MD)^2 + (\lambda_3 - MD)^2]}{2(\lambda_1^2 + \lambda_2^2 + \lambda_3^2)}}.$$

Chapter 3

Mathematical Model
for Brain Tumors

In this chapter a mathematical model is introduced for modeling tumor growth. In this thesis, the focus is modeling of tumor growth in the brain. Fick's law of diffusion is used to get the reaction-diffusion equation. A Neumann boundary conditions is imposed and an initial condition is established to provide a realistic starting point for the model.

3.1   Domain

The domain of our system is $\Omega \subset \mathbb{R}^3$, which represents the anatomical brain enclosed by the skull. The brain has a very complex structure and is heterogeneous. In this model, we assume that the tumor can only grow in the white matter and gray matter. Therefore, define the domain in the model such that $\Omega = \Omega_w \cup \Omega_g$, where Ω_w is the region of the brain containing white matter and Ω_g is the region of the brain containing gray matter. The partitioning of the domain in this manner allows us to accurately capture the distinct physiological characteristics of these two types of brain tissue, which can be crucial in understanding the dynamics of tumor growth within the brain. This approach to defining the domain of the mathematical model aligns with the methodologies outlined in the work of Murray [18].

3.2   Reaction-Diffusion Equation
via Laplace Operator Δ

We assume that growth of glioma tumor cells is governed by proliferation and diffusion. Proliferation takes into account cell division. Here, diffusion is used to

approximate tumor cell motility. We will then use the reaction diffusion equation

$$\frac{\partial u(x,t)}{\partial t} = \nabla \cdot (D(x)\nabla u(x,t)) + f(u(x,t)) \text{ in } \Omega \times (0,T), \qquad (3.1)$$

where the left-hand side describes how a quantity changes over time and the right-hand side describes the spatial evolution of that quantity. If we let $u = u(x,t)$ be the cell density in Ω at time $t \in [0,T]$, the mass m of the tumor inside Ω is then given by the volume integral

$$m(t) = \int_{\Omega} u(x,t)\,dx. \qquad (3.2)$$

To take into account cell division and cell death the term $f(u)$ is introduced so that the net proliferation rate is given by

$$\frac{dm_f}{dt} = \int_{\Omega} f(u(x,t))\,dx \qquad (3.3)$$

It is assumed that the cells diffuse according to Fick's law of diffusion. It states that particles move from high concentrations to low concentrations and the flux points to the most rapid decreasing direction of the cell density. Mathematically the flux J is described by

$$J(x,t) = -D(x)\nabla u(x,t), \qquad (3.4)$$

where ∇ is the gradient operator and $D(x)$ is the diffusion coefficient. The total flux across the boundary $S = \partial\Omega$ is given by

$$\frac{dm_{flux}}{dt} = -\int_{S} J(x,t) \cdot n(x)\,dS, \qquad (3.5)$$

where $n(x)$ is the outward unit vector normal to S. By the divergence theorem we have

$$-\int_{S} J(x,t) \cdot n(x)\,dS = \int_{\Omega} \nabla \cdot J(x,t)\,dx. \qquad (3.6)$$

Equations (3.3) and (3.5) can be put together as a balance equation

$$\frac{dm_{tot}}{dt} = \frac{dm_{flux}}{dt} + \frac{dm_f}{dt}, \qquad (3.7)$$

where m_{tot} is the total mass in Ω, m_{flux} refers to the mass that is diffusing inside Ω, and m_f refers to the net mass that is generating in Ω. Therefore, by combining (3.2)–(3.7) we obtain

$$\frac{d}{dt} \int_{\Omega} u(x,t)\,dx = \int_{\Omega} \nabla \cdot (D(x)\nabla u(x,t))\,dx + \int_{\Omega} f(u(x,t))\,dx. \qquad (3.8)$$

Assuming (3.1) to be true, then (3.8) holds. Note that equation (3.1) does not capture the bio-mechanical properties of the brain and therefore there is not any deformation of the brain.

3.2.1 Boundary and Initial Condition

We impose the Neumann boundary condition

$$D(x)\nabla u(x,t) \cdot n(x) = 0 \quad \text{on} \quad S \times (0,T), \tag{3.9}$$

where $n(x)$ is the outward normal unit vector to the boundary S. The boundary condition states that tumor cells never leave, or come from outside of Ω. We assume an initial cell density at time $t = 0$ for the model is

$$u(x,0) = \phi(x) \quad \text{in} \quad \Omega. \tag{3.10}$$

The initial condition $\phi(x)$ (seed) is usually assumed to have the form

$$\phi(x) = e^{-(x-x_0)^2/d^2}, \tag{3.11}$$

where $d > 0$ and x_0 is the center of the seed, as in [22, 21] as well as others. Such an assumption stems from the fact that there is no information of initial tumor cell density from MR images alone.

In this thesis, we will use both (3.11) and an initial tumor cell density with the help of histology images. It is important to note that with this initial condition, it is assumed that the tumor has grown already to that size and starts to diffuse.

3.3 Proliferation

The term $f(u)$ in equation (3.1) can be thought of as the net proliferation rate of the tumor cells. To model the proliferation, we consider the generalized logistic function

$$f(u) = \rho u^\alpha (1 - u^\beta), \tag{3.12}$$

where α, β, and ρ are positive constants. It is of interest to investigate what values of these constants give realistic results, if at all. In related works, see [18, 22], it is assumed that $\alpha = \beta = 1$.

To get a sense of the behavior of the proliferation term, we study the ordinary differential equation (ODE)

$$\frac{dw(t)}{dt} = f(w), \tag{3.13}$$

where $w(t)$ is some unknown quantity. One obtains exponential growth in case $f(w) = \rho u$, i.e the solution to (3.13) is

$$w(t) = w_0 e^{\rho t},$$

where $w_0 = w(0)$ is an initial condition. This is not realistic tumor growth since $w \to \infty$ as $t \to \infty$. A more realistic tumor growth is expected with parameters $\alpha = 1$ and $\beta = 1$, which is called the logistic growth. The solution to (3.13) is

$$w(t) = \frac{w_0}{w_0 + (1 - w_0)e^{-\rho t}}.$$

However, it is interesting to investigate whether $\beta \neq 1$ can model cancer growth better. Assuming $\alpha = 1$ and $\beta > 0$, the solution to (3.13) becomes

$$w(t) = \frac{1}{(1 + Ke^{-\beta \rho t})^{1/\beta}},$$

where $K = -1 + 1/w_0^\beta$. In Figure 3.1 we can see the behavior of $w(t)$ for some different values of β. From the figure we can observe that the quantity $w(t)$ grows
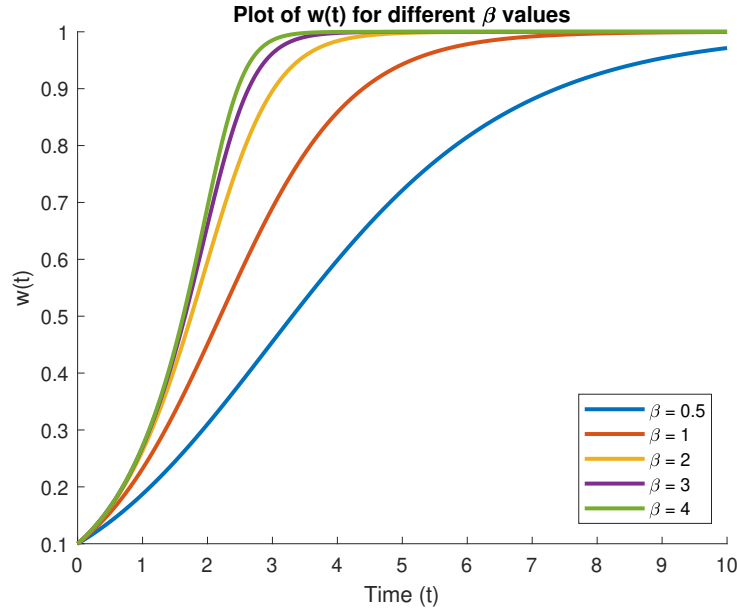
Figure 3.1: The solution to the ODE (3.13) with generalized logistic function term for different values of β.

more rapidly as β increases. In this thesis, tumor growth of HGG is modelled with $\alpha = 1$, and $\beta = 2$.

In other works such as [11, 15], $\beta = 1$ is used to model a logistic growth of brain tumors, [15] uses $\beta = 1$ to model LGG glioma growth. However, the choice of β is not necessarily limited to this value, and it is plausible that the growth of HGG gliomas could be more rapid. Hence, it would be worthwhile to explore a different value of β.

Necrosis and Space Variance

In reality, tumor cells begin to change to necrosis, a form of cell death due to insufficient nourishment. This phenomenon is a critical aspect of tumor growth and progression, and should be incorporated into tumor growth mathematical models to improve its accuracy and realism. A simplifying assumption made so far is that the cell proliferation rate, denoted as ρ, is space-independent. However,

in reality, ρ can vary across different regions within the tumor [6]. The space variance of ρ is implemented in this thesis, see Section 4.6.

3.4 Diffusion Matrix

In [17], the diffusion matrix is a diagonal matrix in the form $D = dI$, where $d > 0$ and I is the identity matrix. This works only on a homogeneous brain, that is, tumor cells diffuse equally across the brain region Ω. As [18] points out, tumor cells diffuse at different rates between the two main regions of the brain, white matter and gray matter. The diffusion matrix is then changed to incorporate this observation by making it spatially dependent such that

$$D(x) = \begin{cases} D_g I & \text{for } x \in \Omega_g\,, \\ D_w I & \text{for } x \in \Omega_w\,, \end{cases} \tag{3.14}$$

where $D_w > 0$ is the diffusion coefficient in white matter tissue and $D_g > 0$ is the diffusion coefficient in gray matter tissue. This type of diffusion will be called *bimodal diffusion* in this thesis. According to [18] it can be assumed that $D_w \approx 5D_g$. The reaction-diffusion (1.2) with the diffusion matrix (3.14) is the model used in [18], [10]. In this thesis, a new diffusion matrix is defined

$$D(x) = c(x)D_w I + (1 - c(x))D_g I, \tag{3.15}$$

where $c(x)$ is between 0 and 1 and is based on the intensity of MR images. This type of diffusion will be called *gradient diffusion*. In T_2-w images, where gray matter appears brighter than white matter, Equation (3.16) becomes

$$D(x) = c(x)D_g I + (1 - c(x))D_w I. \tag{3.16}$$

Both the bimodal diffusion and gradient diffusion will be used and the results are compared in Chapter 5.

Let the intensity value of a voxel be denoted as $V(x)$. The goal is to transform this value into a normalized intensity, which is represented as $c(x)$. The mathematical representation of this process starts with identifying the minimum and maximum values within the original volume

$$V_{\min} = \min_{x \in \Omega} V(x), \quad V_{\max} = \max_{x \in \Omega} V(x).$$

The normalized intensity value is obtained by dividing each element in the shifted volume by the range, i.e.,

$$c(x) = \frac{V(x) - V_{\min}}{V_{\max} - V_{\min}}.$$

However, the normalization process assumes that the brain region Ω has already been defined so that CSF and the ventricles (where tumor growth does not occur) can be disregarded. Segmentation is used to identify and exclude these regions from the analysis, as detailed in the materials and methods section. This approach is similar to the methodology described in [27].

3.5 Reaction-Diffusion Equation via p-Laplace Operator Δ_p

It can be useful to investigate how the model behaves when the p-Laplace operator is introduced [16], in particular with $1 < p \le 2$. The p-Laplace operator is defined as

$$\Delta_p u(x) = \nabla \cdot \left(|\nabla u(x)|^{p-2} \nabla u(x) \right), \tag{3.17}$$

where $x \in \mathbb{R}^3$ and $|\nabla u|$ is defined as

$$|\nabla u| = \left[\left(\frac{\partial u}{\partial x_1} \right)^2 + \left(\frac{\partial u}{\partial x_2} \right)^2 + \left(\frac{\partial u}{\partial x_3} \right)^2 \right]^{\frac{1}{2}}. \tag{3.18}$$

Using (3.17), a general reaction-diffusion equation via the p-Laplace operator can be constructed

$$\frac{\partial u(x,t)}{\partial t} = \nabla \cdot \left(D(x) |\nabla u|^{p-2} \nabla u(x,t) \right) + f\left(u(x,t) \right). \tag{3.19}$$

This is a non-linear PDE, which is hard to solve with standard methods. Furthermore, it introduces singularities when $|\nabla u| = 0$. Figures 3.2–3.4 illustrate the effect of the p-Laplace operator on tumor growth simulations for three different diffusion matrices at $T = 60$, each solved for three different p-values and $f(u(x,t)) = \rho u(1 - u^2)$. The domain is a a $50 \times 50 \times 50$ cube and the bimodal diffusion is used. The parameters used for this simulation experiment are $D_w = 0.5$, $D_g = 0.1$, $\rho = 0.085$, and $u_0^* = 0.9$ with a time step $\Delta t = 0.05$.
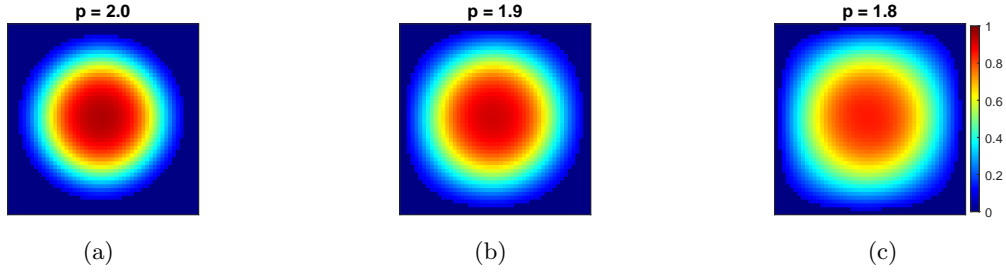
Figure 3.2: Simulation has constant diffusion coefficient of 0.5.
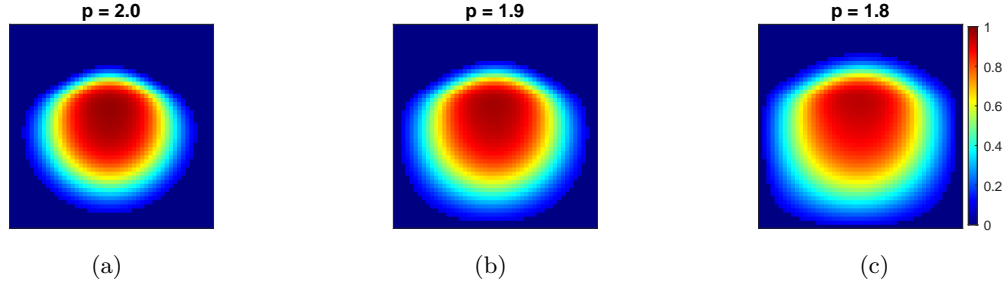
Figure 3.3: From the 32nd to the 50th layer, the diffusion coefficient is set at 0.1. For the 25th to the 31st layer, we set zones of progressively lower diffusion coefficient, ranging from 0.2 to 0.5.
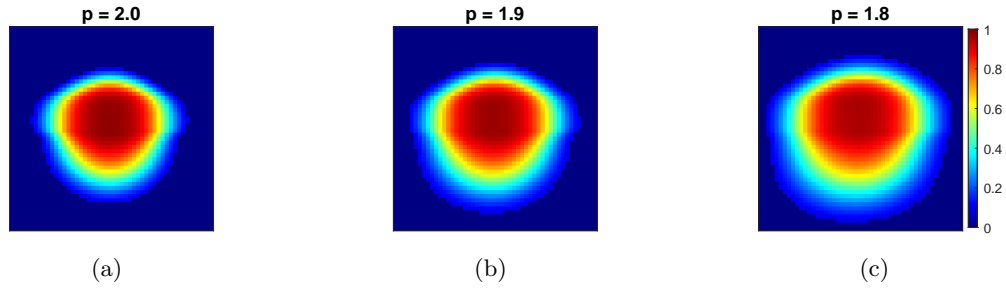
Figure 3.4: The same progression happens above the middle layer, and below the middle layer but in reverse.

Chapter 4

Materials and Methods

4.1 Data

The datasets used in this thesis are the University of Pennsylvania glioblastoma (UPenn-GBM) [1, 2, 5] and IVY Glioblastoma Atlas Project (IvyGAP) [4]. The UPenn-GMB dataset contains MR images such as T_1-w, T_2-w, and DTI, of patients diagnosed with a brain tumor. T_1-w images are used to segment the brain into white matter, gray matter and CSF. The UPenn-GBM dataset also includes tumor segmentations, both automatic performed by a computer and manually performed by clinicians. In this thesis, we only use the automatic segmentation to avoid biases. An example of the tumor segmentation can be seen in Figure 4.1
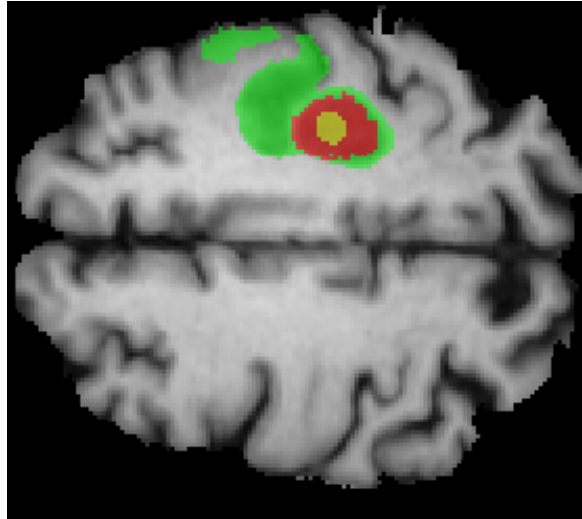
Figure 4.1: Example of tumor segmentation from the UPenn-GBM dataset in a T_1-w image [1]. The green highlights edema/invasion, red highlights the tumor enhancement and yellow highlights the necrosis.

The tumor segmentations are compared with our synthetic tumor. The methodology is described in the evaluation section of this chapter. The UPenn-GBM dataset has more than 600 patients, but in this thesis we only use four for simulations, and from the IvyGAP-dataset one patient is used for incorporating histology (Table 4.1). Clinical and radiomic data for patients can also be found in [2].

Table 4.1: Data used in this thesis for the simulations.

Dataset	T_1-w, T_2-w	ADC	Histology	Segmentations	Patient
UPenn-GBM	Yes	Yes	No	Yes	1-4
IvyGAP	Yes	No	Yes	Yes	5

4.2 Data Pre-Processing

To compute the diffusion matrix in the implementation code, it is necessary to segment the brain into white matter, gray matter and CSF. For this we use the FMRIB's automated segmentation tool (FAST) in the FMRIB Software Library (FSL) [28, 12]. The results of using FAST on a T_1-w image with a tumor is shown in Figure 4.2. It is clear that the segmentation inside the red circle is inaccurate and does not provide us with useful information about the tumor. In addition, any
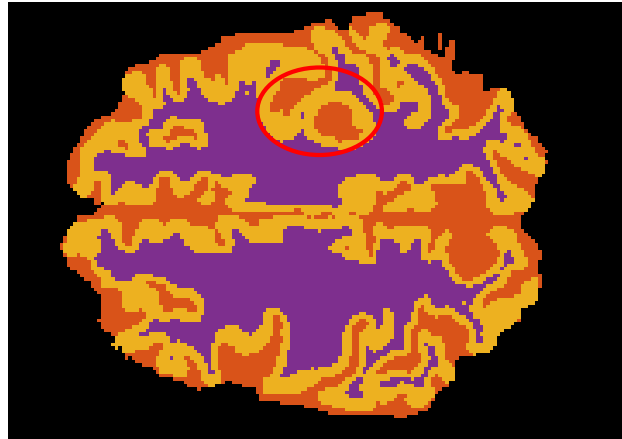
Figure 4.2: An example of brain structure segmentation with FSL. Purple is white matter, yellow is gray matter and orange is CSF. Encircled with red is the location of the tumor. FSL wrongly classifies the tumor as CSF or gray matter.

information about white matter, gray matter and CSF is lost in the affected area. To take this into account, we take advantage of the symmetry of the brain. The segmentation is performed on the healthy half of the brain to avoid any additional errors in the segmentation. Then the healthy half of the brain is mirrored (Figure

4.3), and a seed of a tumor is then planted in the white matter approximately into the mirrored area of the tumor.
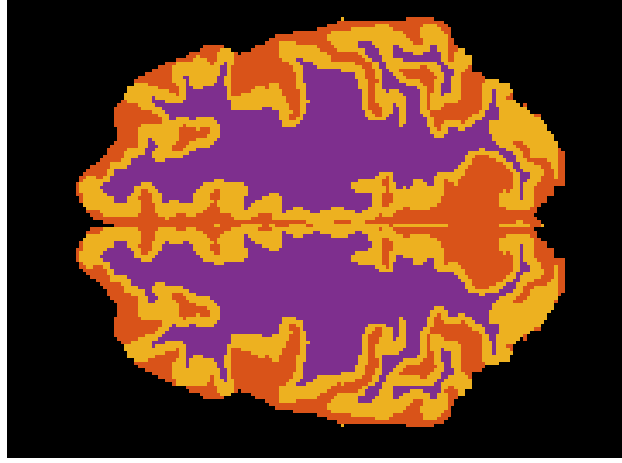
Figure 4.3: Mirrored brain.

4.3 Numerical methods

We solve (3.1) using MATLAB by following the numerical implementation in [10]. The model can be written as

$$\frac{\partial}{\partial t}u(x,t) = A(x)u(x,t) + f\big(u(x,t)\big), \tag{4.1}$$

where A is a differential operator so that the first term on the RHS corresponds to the term $\nabla \cdot (D(x)\nabla u(x,t))$ of (3.1). We partition our time domain $[0,T]$, $T > 0$, in $N+1$ equally spaced points

$$0 = t_0 < t_1 < t_2 < ... < t_N = T.$$

The time derivative is approximated with the Euler forward method, this gives us

$$u^{i+1}(x) = u^i(x) + \Delta t\big(A(x)u^i(x) + f(u^i(x))\big),$$

where $i \in \{0,1,2...,N-1\}$, $\Delta t > 0$ is the step-size in time, and $u^i = u(x,t_i)$. The spatial derivatives in A are approximated using finite differences. The space domain Ω is partitioned in equally spaced points, K points in the the x-direction, L points in the y-direction, and M in the z-direction, forming a 3D-lattice

$$x_0 < x_1 < x_2 < ... < x_{K-1},$$
$$y_0 < y_1 < y_2 < ... < y_{L-1},$$
$$z_0 < z_1 < z_2 < ... < z_{M-1}.$$

Define the forward finite difference with the operator ∂_x^+ and the backward finite difference with the operator ∂_x^- in the x-direction

$$\partial_x^+ u^i(x, y, z) = \frac{1}{h} \big(u^i(x + h, y, z) - u^i(x, y, z) \big),$$
$$\partial_x^- u^i(x, y, z) = \frac{1}{h} \big(u^i(x, y, z) - u^i(x - h, y, z) \big),$$

where $h > 0$ is a step-size in space. Then the second order difference in the x-direction is approximated by the alternating schema

$$\partial_x(d_{11} \partial u^i) = \frac{1}{2} \big(\partial_x^- (d_{11} \partial_x^+ u^i) + \partial_x^+ (d_{11} \partial_x^- u^i) \big)$$

where d_{11} corresponding to the first diagonal elements of D.

The difference operators along the $y-$ and z-direction are defined analogously.

4.3.1 Thresholds and Normalization

Initial Condition

When implementing the initial condition, a threshold value, u_0^* is chosen in order to confine cells in a small volume. In this thesis, the value of $u_0^* = 0.9$ is used for all the simulations, where the Gaussian seed (3.11) was planted. It is clear that it has an effect on the number of iterations needed for the simulated tumor to reach a certain volume. If the threshold is too small then the simulation starts with a very big tumor, whilst if the threshold is close to 1, then we get a very small initial tumor, and it might not have the time to grow since it can diffuse a lot faster than it proliferates. The placement of the seed is determined by calculating the centroid of the segmented tumor, which is denoted as x_0.

Gradient Diffusion

For the case where we use an MR intensity based diffusion matrix, first, the intensity voxel values are normalized as described in Section 3.4. Since the black background voxels should not be counted in the normalization, the segmentation for white matter and gray matter is used to find $V_{\min}$ and $V_{\max}$.

Tumor Detection Threshold

A threshold is introduced based on the simulated tumors cell density $u(x, t)$. If $u(x, t) > 0.16$, determining whether a voxel represents tumor tissue. The use of this threshold, corresponding approximately to the percentage of tumor cells being detectable by T_2-w images, is motivated in [23].

4.4 Evaluation

The Jaccard index is used as a measure to compare the simulated tumor and the ground truth. A similar approach is employed in [2] to compare their anisotropic model with the model in [22]. The Jaccard index measures the similarity between two sets. For any two finite sets A_1 and A_2, the Jaccard index is defined as:

$$J(A_1, A_2) = \frac{|A_1 \cap A_2|}{|A_1 \cup A_2|},$$

where a ratio of 0 means that the two sets have nothing in common, while a ratio of 1 means that the two sets are identical.

4.5 Histology

Histology is the knowledge of examining the organization and arrangement of cells, tissues, and organs at a microscopic level to better understand their function, structure, and potential abnormalities or diseases. Tissue samples are obtained through biopsy, surgery, or autopsy. Histology images can aid us to approximate initial tumor cell densities that can be used in our model.

4.5.1 Initial tumor cell density condition

The initial cell density of the tumor is determined by the condition (3.10). However, in the absence of data, an estimation must be made for the function $\phi(x)$. This initial cell density is concentrated within a very small volume and in the the model the assumption is that the function $\phi(x)$ takes the form (3.11).

The IvyGAP database [4] has both histology and MR data which is used in this section. The tumors are subdivided into blocks and labeled with letters, for example as in Figure 4.4. One patient from this dataset is included. Hematoxylin and eosin (H&E) images from three different blocks are selected. By using the software QuPath [3], cells are detected and a heat map is generated, representing tumor cell density, see Figure 4.5. The maximum cells detected per pixel area is found in the red region, and the minimum is found on the dark blue/black region of the heat map in Figure 4.5. The maximum number of detected cells per pixel area is approximately 0.011, and the minimum is approximately 0.0009. In the green region, the value is around 0.0025. Thus, it can be assumed that cell density $u(x,t)$ values close to 1 correspond to the maximum value of cells detected per pixel area for this specific tumor slice of patient 5.

The acquired heat map images from QuPath is processed using MATLAB to enhance color values and convert them into matrices, as QuPath lacks this functionality. The resulting matrices are then resized to smaller dimensions, specifically to a size of 9×9. These resized matrices are used to create slices, which are inserted into a larger empty $9 \times 9 \times 9$ array. The remaining sections of the array are

(a)   (b)
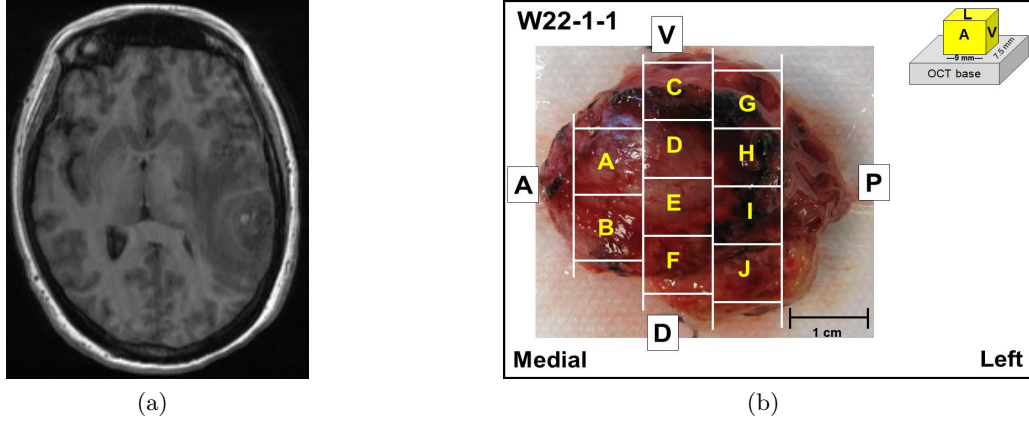
Figure 4.4: (a) T_1-w image of patient 5 (b) Resected tumor of patient 5 [4].

(a)   (b)   (c)
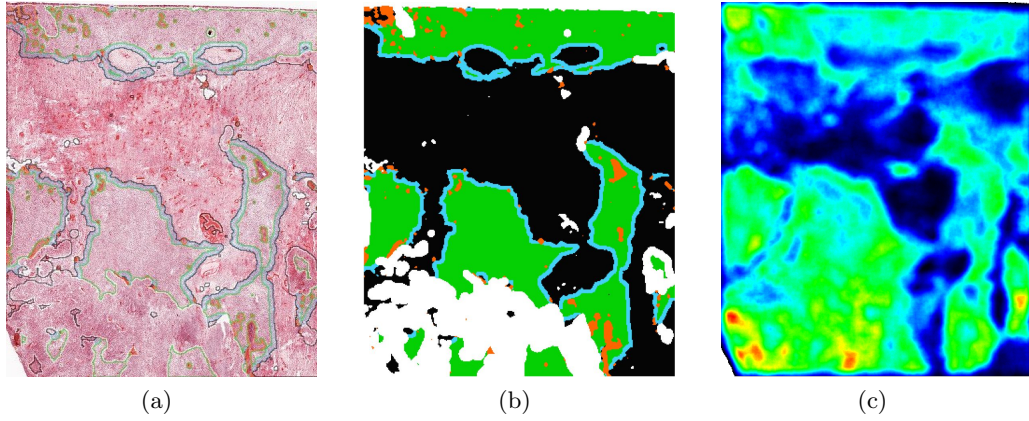
Figure 4.5: (a) H&E image with feature boundaries from a slice of the resected tumor, (b) Tumor annotation for corresponding H&E image, black is necrosis, green is cellular tumor, blue is perinecrotic tumor and orange is blood vessel, (c) Cell density heat map of corresponding H&E image [4].

obtained by interpolation to fill in the gaps. Figure 4.6 illustrates the difference between the two different initial conditions.

4.5.2 Proliferation Index

In [6], the authors investigate the changes in proliferating cell nuclear antigen (PCNA) expression in glioblastoma cells along a stereotactic biopsy (a minimally invasive procedure used to obtain tissue samples) trajectory. These trajectories refer to the paths taken by the probe to reach different regions within the tumor. PCNA is used to stain cells to visualize and quantify the number of proliferating

(a)   (b)
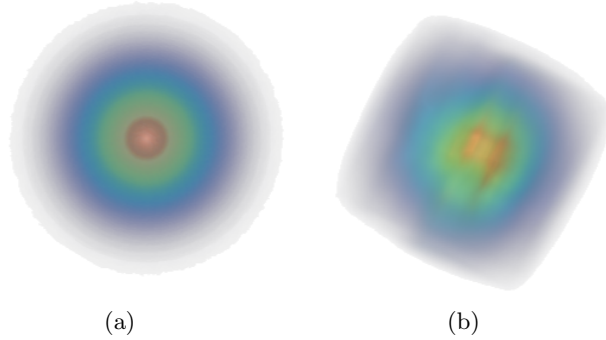
Figure 4.6: (a) Initial condition $\phi(x)$ constructed using (3.11), (b) initial condition $\phi(x)$ constructed using three different slices from H&E stained images.

cells in different regions of the tumor. The proliferation index is calculated as the ratio of observed active proliferating cells and total cancer cells. Table 4.3 shows the median, mean and standard deviation of this ration at different levels in the tumor. Level 0 refers to the beginning of the solid tumor. A negative level is proximal along the trajectory and positive distal along the trajectory. The results suggest that the proliferation rate is spatially dependent.

Unfortunately, calculations as in [6] cannot be performed since it is not possible to see the actively proliferating cells from the IvyGAP database histology images, or any other histology dataset. For this reason, we take similar values as in [6].

It is important to note that the approach of having fixed levels along the biopsy trajectory has limitations. Tumor subregions can vary significantly from patient to patient, making it important to adjust these levels to the individual patient. This method makes a clear distinction for the solid tumor. However, no other information about the tumor is provided. Therefore, the cell proliferation indices with regard to the position alone are not accurate measures. The authors in [6] provide another table that looks at the mean, median and standard deviation with respect to CT-scans, see Table 4.3. These values help us define the proliferation rate.

Table 4.2: Proliferating index with respect to biopsy level [6].

Level	Mean	Median	Standard Deviation
-20mm	0.47	0.38	0.47
-10mm	1.95	0.66	3.45
0	7.02	5.45	6.26
+10mm	1.98	0.39	2.62
+20mm	0.19	0.09	0.31

Table 4.3: Proliferating index with respect to radiographic appearance [6]. PH = region of hypodensity on CT-image, CE = contrast enhancing region, CH = region of hypodensity on the CT-image within the contrast-enhancing region of tumor.

Level	Mean	Median	Standard Deviation
PH	0.90	0.38	1.43
CE	3.91	1.38	5.98
CH	4.31	2.67	4.92

4.6 Implementation of Spatially Varying Proliferation Index

Inspired by [6], the space varying proliferation rate $\rho = \rho(x)$ can be implemented by dividing the tumor into two parts, see Figure 4.7. The radius r_0 corresponds to the level PH, r_1 to the levels PH and CE.

Note that both r_0 and r_1 must be time dependent, otherwise the tumor would not grow. This, in turn makes the proliferation rate time dependent as well. The histology images provided by the IvyGAP dataset do not provide sufficient information for an approximation of the proliferation rate. Therefore, the values obtained from [6] act as a useful reference for selecting appropriate proliferation rates.

The necrotic region of a brain tumor in an MR image can be represented by the radius denoted as r_0, which can be extracted from the MR images. On the other hand, the second radius, denoted as r_1, can be estimated using MR images as an approximation. The focus in this thesis is primarily on utilizing these radii to define the spatially varying proliferation rate, and therefore r_0 is not considered as necrotic tissue.
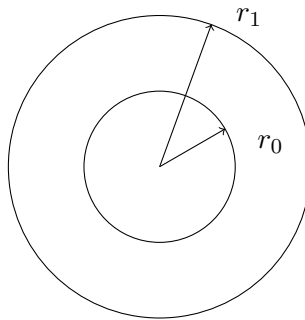
Figure 4.7: Tumor divided into two different regions defined by the radii r_0 and r_1.

For the simulations, the thresholds $r_0 = 0.4R$ and $r_1 = 0.7R$ are used, where R is the current radius of the tumor. These thresholds are selected by trial and

error. The spatially varying proliferation is given by

$$\rho(x) = \begin{cases} 0.04 & \text{for} \quad |x - x_0| \leq r_0, \\ 0.08 & \text{for} \quad r_0 < |x - x_0| \leq r_1, \\ 0.05 & \text{for} \quad |x - x_0| > r_1 \end{cases} \tag{4.2}$$

where x_0 is the point of the center of the planted seed. When trying to use similar values to the median in Table 4.3, the tumor starts growing in the region $r_0 < |x - x_0| < r_1$ prior to developing within the region $|x - x_0| \leq r_0$ which is not realistic. Therefore the values $(0.04, 0.08, 0.05)$ are used.

Chapter 5

Results

This chapter presents the results of the thesis for five patients, which includes tumor simulations on T_1-w, T_2-w and ADC images with two different diffusion matrices (bimodal and gradient diffusion matrix). Heat maps of simulated tumors with the best and worst Jaccard index (JI) are also provided for patient 1. The segmented (ground truth) tumor is shown in red, while the simulated tumor is shown in green and yellow. The yellow color indicates the overlap between the simulated and segmented tumor, and the green color represents the non-overlapping portion of the simulated tumor with the segmentation.

In addition to the images, tables are provided for the different diffusion matrices used on three different MR modalities, T_1-w, T_2-w, and ADC images, as well as 3 different p-values, showing the maximum JI and the corresponding iteration at which the maximum is achieved. These tables provide a quantitative evaluation of the tumor simulation performance using the bimodal and gradient diffusion matrices. The number of iterations needed to reach maximum JI is also shown.

For the bimodal diffusion matrix, the T_1-w image is used for the segmentation of white matter, gray matter and CSF. Therefore, no calculation is performed for other modalities since the segmentation was similar to the one from T_1-w.

Two main observations can be made from the tables in this chapter. The first observation is that the JI is higher when using the gradient diffusion matrix than when using the bimodal diffusion matrix. The second observation is for T_1-w images, we always get a somewhat higher JI for $p = 1.8$. Even when varying the parameters D_w, D_g and ρ, see Tables 5.2–5.7, we still get a higher JI on T_1-w images.

Figures 5.1–5.4 illustrate the differences between the ground truth and the simulated tumor and the simulated cell density $u(x, t)$. In Figures 5.3 and 5.4, we can observe that the tumor cell density is lower than that in Figure 5.1. The shape of the tumor however is very similar for all cases shown. Similar results are seen for the rest of the patients; therefore, only the best results are summarized in Table 5.8 for these patients.

Figure 5.5 illustrates the differences between the ground truth and the sim-

ulated tumor with an initial condition constructed from H&E stained histology images. There are subtle difference but the overall shape stays the same compared to Figures 5.1–5.4.

Figure 5.6 illustrates how the radius of the simulated tumor grows with respect to the iterations. The radius of the simulated tumor is observed to be close to spherical and therefore an average radius from the planted seed point is calculated.

Table 5.1: Results for patient 1 with different p values. The parameters used are: $D_w = 0.5$, $D_g = 0.1$, $\rho = 0.04$, $u_0^* = 0.9$.

| MR modality | p value | D bimodal (3.14) | | D gradient (3.16) | |
		JI	Iteration	JI	Iteration
T_1-w	2	0.4382	1764	0.4498	1686
T_2-w	2	-	-	0.4550	1638
ADC	2	-	-	0.4557	1663
T_1-w	1.9	0.4511	1690	0.4581	1658
T_2-w	1.9	-	-	0.4617	1677
ADC	1.9	-	-	0.4623	1693
T_1-w	1.8	0.4628	1718	0.4720	1658
T_2-w	1.8	-	-	0.4617	1811
ADC	1.8	-	-	0.4398	1838

Table 5.2: Results for patient 1 with different p values. The parameters used are: $D_w = 0.51$, $D_g = 0.1$, $\rho = 0.04$, $u_0^* = 0.9$.

| MR modality | p value | D bimodal (3.14) | | D gradient (3.16) | |
		JI	Iteration	JI	Iteration
T_1-w	2	0.4389	1759	0.4501	1681
T_2-w	2	-	-	0.4547	1634
ADC	2	-	-	0.4557	1663
T_1-w	1.9	0.4515	1692	0.4590	1627
T_2-w	1.9	-	-	0.4624	1680
ADC	1.9	-	-	0.4623	1683
T_1-w	1.8	0.4627	1728	0.4726	1653
T_2-w	1.8	-	-	0.4598	1825
ADC	1.8	-	-	0.4444	1907

Table 5.3: Results for patient 1 with different p values. The parameters used are: $D_w = 0.52$, $D_g = 0.1$, $\rho = 0.04$, $u_0^* = 0.9$.

MR modality	p value	D bimodal (3.14)		D gradient (3.16)	
		JI	Iteration	JI	Iteration
T_1-w	2	0.4337	1470	0.4503	1674
T_2-w	2	-	-	0.4550	1635
ADC	2	-	-	0.4558	1783
T_1-w	1.9	0.4472	1360	0.4600	1626
T_2-w	1.9	-	-	0.4624	1681
ADC	1.9	-	-	0.4630	1690
T_1-w	1.8	0.4612	1364	0.4733	1670
T_2-w	1.8	-	-	0.4576	2242
ADC	1.8	-	-	0.4393	2371

Table 5.4: Results for patient 1 with different p values. The parameters used are: $D_w = 0.60$, $D_g = 0.1$, $\rho = 0.04$, $u_0^* = 0.9$.

MR modality	p value	D bimodal (3.14)		D gradient (3.16)	
		JI	Iteration	JI	Iteration
T_1-w	2	0.4458	1748	0.4520	1683
T_2-w	2	-	-	0.4564	1670
ADC	2	-	-	0.4393	1920
T_1-w	1.9	0.4575	1744	0.4624	1637
T_2-w	1.9	-	-	0.4658	1681
ADC	1.9	-	-	0.4563	1744
T_1-w	1.8	0.4579	1781	0.4740	1670
T_2-w	1.8	-	-	0.4293	1950
ADC	1.8	-	-	0.4002	2018

Table 5.5: Results for patient 1 with different p values. The parameters used are: $D_w = 0.5$, $D_g = 0.09$, $\rho = 0.04$, $u_0^* = 0.9$.

MR modality	p value	D bimodal (3.14)		D gradient (3.16)	
		JI	Iteration	JI	Iteration
T_1-w	2	0.4393	1777	0.4490	1688
T_2-w	2	-	-	0.4551	1638
ADC	2	-	-	0.4556	1662
T_1-w	1.9	0.4528	1695	0.4580	1591
T_2-w	1.9	-	-	0.4616	1671
ADC	1.9	-	-	0.4623	1691
T_1-w	1.8	0.4652	1720	0.4722	1652
T_2-w	1.8	-	-	0.4621	1808
ADC	1.8	-	-	0.4490	1877

Table 5.6: Results for patient 1 with different p values. The parameters used are: $D_w = 0.5$, $D_g = 0.05$, $\rho = 0.04$, $u_0^* = 0.9$.

MR modality	p value	D bimodal (3.14)		D gradient (3.16)	
		JI	Iteration	JI	Iteration
T_1-w	2	0.4380	1869	0.4461	1708
T_2-w	2	-	-	0.4548	1645
ADC	2	-	-	0.4555	1652
T_1-w	1.9	0.4559	1770	0.4572	1596
T_2-w	1.9	-	-	0.4618	1674
ADC	1.9	-	-	0.4624	1682
T_1-w	1.8	0.4742	1752	0.4705	1610
T_2-w	1.8	-	-	0.4644	1765
ADC	1.8	-	-	0.4533	1858

Table 5.7: Results for patient 1 with different p values. The parameters used are: $D_w = 0.5$, $D_g = 0.1$, $\rho = (0.04, 0.08, 0.05)$, $u_0^* = 0.9$.

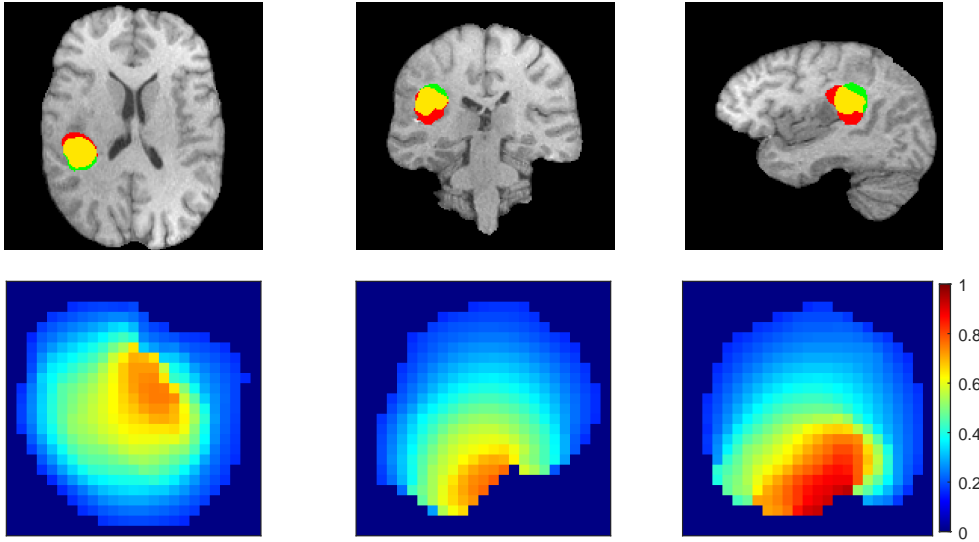| MR modality	p value	D bimodal (3.14)		D gradient (3.16)	
		JI	Iteration	JI	Iteration
T_1-w	2	0.3371	1280	0.4447	973
T_2-w	2	-	-	0.4464	1015
ADC	2	-	-	0.4473	991
T_1-w	1.9	0.3283	1265	0.4686	974
T_2-w	1.9	-	-	0.4498	928
ADC	1.9	-	-	0.4497	921
T_1-w	1.8	0.3384	1246	0.4724	972
T_2-w	1.8	-	-	0.4642	928
ADC	1.8	-	-	0.4616	977

Figure 5.1: Tumor simulation using a bimodal diffusion matrix with $p = 2$, $D_w = 0.5$, $D_g = 0.1$, $\rho = 0.04$ and $u_0^* = 0.9$.
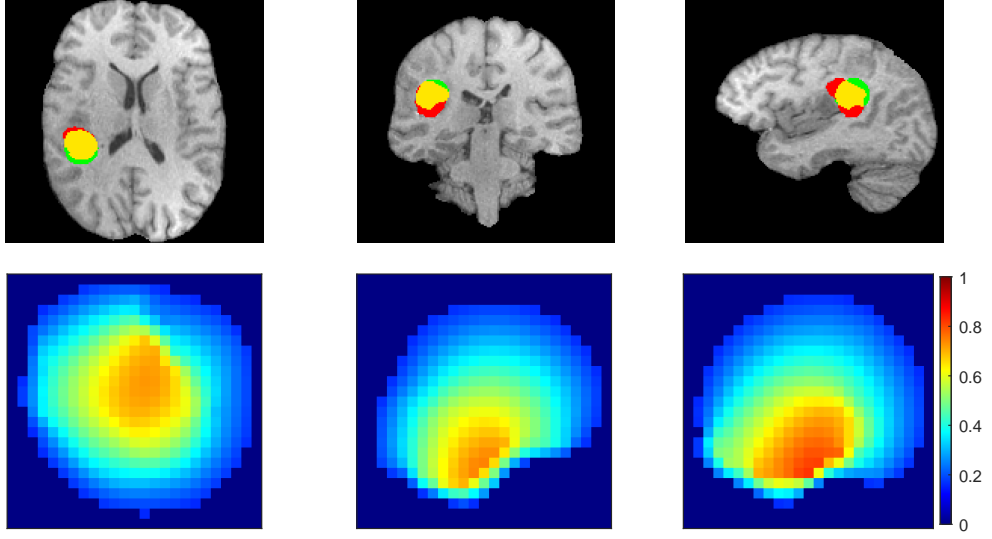
Figure 5.2: Tumor simulation using a gradient diffusion matrix and $p = 2$, $D_w = 0.5$, $D_g = 0.1$, $\rho = 0.04$ and $u_0^* = 0.9$.

Figure 5.3: Tumor simulation on T_1-w images using a gradient diffusion matrix with $p = 1.8$, $D_w = 0.5$, $D_g = 0.1$, $\rho = 0.04$ and $u_0^* = 0.9$.

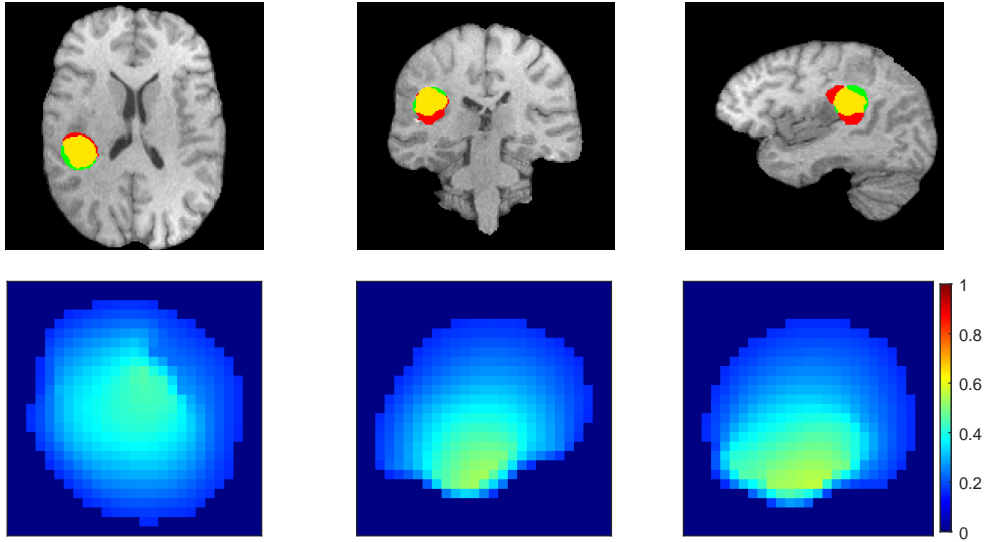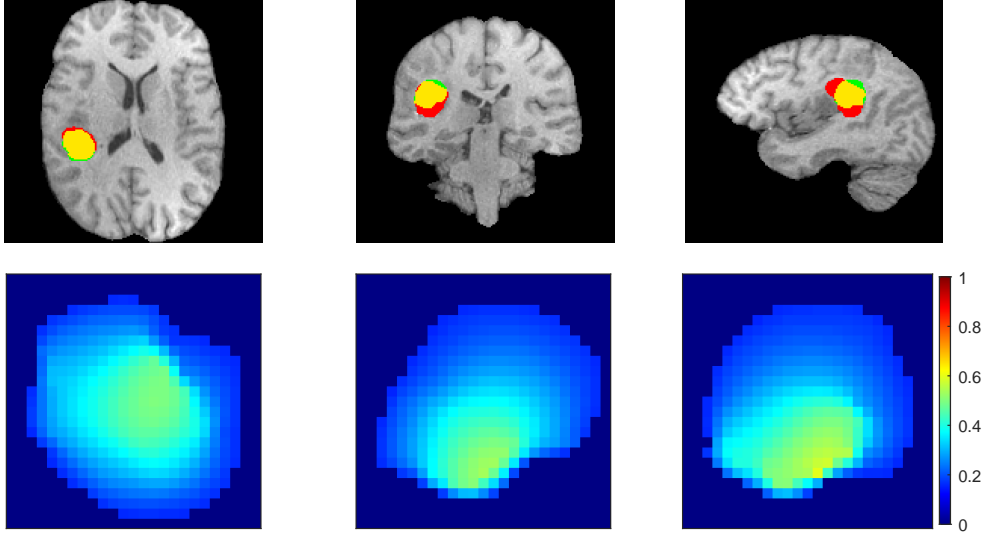Figure 5.4: Tumor simulation using a gradient diffusion matrix and $p = 1.8$, $D_w = 0.5$, $D_g = 0.1$, $\rho = (0.04, 0.08, 0.05)$ and $u_0^* = 0.9$.
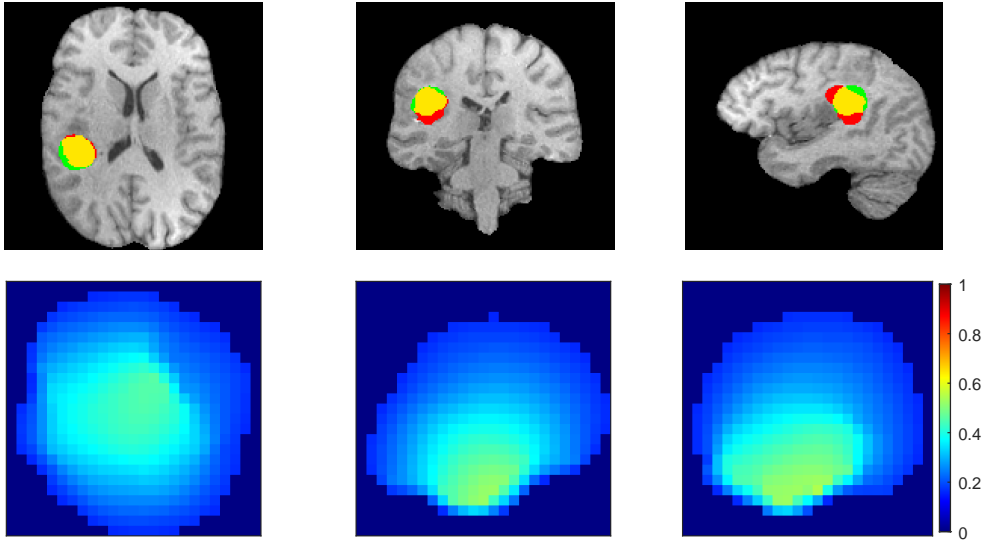
Figure 5.5: Tumor simulation with histology based $\phi(x)$, $p = 1.8$, $D_w = 0.5$, $D_g = 0.1$ and $\rho = 0.04$.
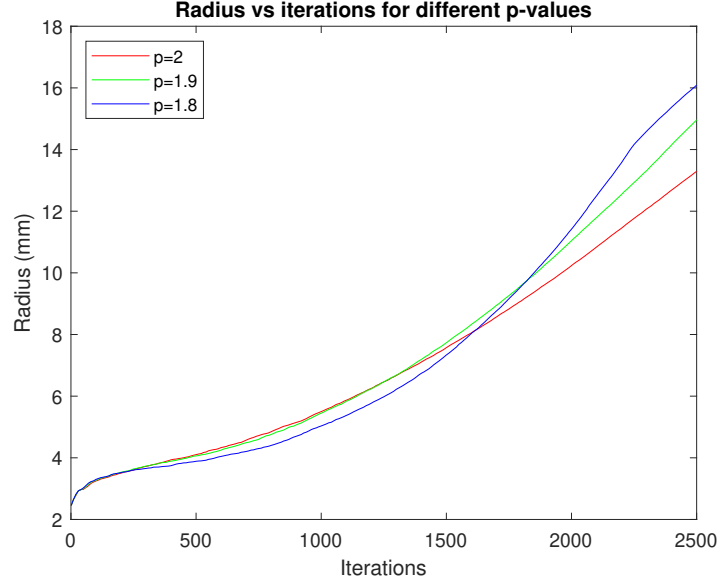
Figure 5.6: Plot of average tumor radius against iteration for three different p-values with gradient diffusion. The parameters use here are $D_w = 0.5$, $D_g = 0.1$, $\rho = 0.04$ and $u_0^* = 0.9$, $\Delta t = 0.05$.

Table 5.8: Summary of best results for patients 1–4 with parameters $D_w = 0.5$, $D_g = 0.1$, $\rho = 0.04$ and $u_0^* = 0.9$.

Patient	Modality	p-value	Diffusion matrix	JI
1	T_1-w	1.8	Gradient diffusion	0.4720
2	T_1-w	1.8	Gradient diffusion	0.4909
3	T_1-w	1.8	Gradient diffusion	0.4325
4	T_1-w	1.9	Gradient diffusion	0.4417

Chapter 6

Discussion

In this chapter, the discussion will revolve around the outcomes of the thesis. The fulfillment of the aim, along with an assessment of the extent to which our results can contribute to research and potential applications in the field is discussed. Furthermore, limitations of this thesis will be taken into account, and future work will be suggested.

6.1   Parameters

The reaction-diffusion equation (1.2), commonly used to model brain tumors, undergoes three key modifications in this thesis. Firstly, the diffusion matrix D incorporates the use of T_1-w, T_2-w, and ADC images through a diffusion matrix (3.16) that relies on the normalized intensity of the MR images. Secondly, the p-Laplace operator is introduced into the model (3.19). Lastly, a spatially varying proliferation rate (4.2) is incorporated.

Tables 5.1–5.7 show an improvement in performance based on the JI index. Notably, the highest JI index is achieved on the T_1-w images when a combination of the convex diffusion matrix and $p = 1.8$ is used. These findings provide valuable insights into the potential efficacy of the proposed modifications to the standard reaction-diffusion model. By incorporating the convex diffusion matrix, p-Laplace operator, and spatially varying proliferation rate, an improved performance is achieved as indicated by the JI, which suggests further investigation into these parameters is needed.

Segmenting the brain structure is not needed when the gradient diffusion (3.16), except when doing the normalization. This of course can be done differently since errors in the segmentation process can lead to inaccuracies on the location of the tumor growth.

Table 5.7 shows that when the proliferation rate varies spatially with the specified parameters values, it takes fewer iterations to reach the maximum JI compared to using a constant proliferation rate. This reduction in iterations is probably due to the specific value assigned to ρ, which is 0.08 within the range $r_0 < r < r_1$. It

is worth noting that the threshold values for r_0 and r_1 were made arbitrarily in this thesis. Further research and experimentations are necessary to validate and optimize the choice of threshold values and assess their impact on the model. It is important to note that the patients selected in this thesis have tumors that have closer to a spherical shape and are not that large to cause big deformations in the brain.

6.2 Time Aspect and Realism of Tumor

The heat maps generated by the model with the gradient diffusion and the p-Laplace operator show a lower tumor cell density compared to the simpler model with the bimodal diffusion and $p = 2$. However, despite this variation in cell density, the overall shape and appearance of the tumor in the heat maps remain very similar. The correspondence between one variable t in the model and real-time is unclear. In [24] it is stated that HGG gliomas have a growth rate of 30 mm/year in diameter. Without this correspondence between one iteration and real time, we cannot extract any growth rate that agrees or disagrees with [24]. Although Figure 5.4 provides some insight in this regard, showing a relationship between simulated tumor radius and iteration, further investigation is required to gain a better understanding. If we however assume that the growth should be 30 mm/year in diameter, then from Figure 5.6, 2500 iterations with time step $\Delta t = 0.05$ correspond to about a year.

The authors in [24] state that the radius of the tumor grows linearly for HGG gliomas which is in agreement with the results for $p = 2$. They also state that the tumor becomes lethal, when it reaches a diameter of around 6cm, which gives a stopping criterion for simulations. As seen in Figure 5.6 for the other two values of p we see something close to an exponential growth. In [20], larger tumors exhibited significantly lower growth rates compared to smaller tumors, exhibiting Gompertzian growth, suggesting that there is a transition in the growth dynamics of tumors as they increase in size and needs to be accounted for in the mathematical model.

6.3 Thresholds

The use of the tumor cell density detection threshold 0.16 dictates whether a voxel classifies as having cancer cells which in turn affects the number of iterations needed to reach the maximum JI. It is possible that another value might be more suitable.

Another threshold that can affect the iterations needed to reach the maximum JI is the choice of u_0^*. Choosing this threshold can be tricky since if it is too small the tumor will diffuse very fast and no voxel will have a tumor cell density above 0.16 so that it can be classified as a tumor voxel. It is certainly possible to optimize this threshold.

The calculated JI depends on these thresholds as well. An observation is that the JI gets smaller in the first couple of iterations and then goes up again, this behavior of the JI is also observed in [21], however, not much explanation is given about it. This suggests that these threshold values of u_0^* and the tumor detection threshold need to be tuned differently to avoid the tumor from shrinking in the beginning of the simulation.

6.4 Limitations

One limitation in this thesis is the lack of MR images of patients before the appearance of a tumor. Having a pre-cancer MR image of the patient would allow us to plant the tumor at the real half of the brain where the tumor appears on the MR image. It is possible that planting the tumor in the "healthy" part of the brain, can have an effect on the JI since the simulated tumor might end up outside the brain region when reflected back to the other half of the brain.

6.5 Future Work

This thesis demonstrates that extracting cell densities from histology images of patients with brain tumors, allows for the creation of an initial condition based on these extracted cell densities. To further increase the model's accuracy, the next stage involves establishing a relationship between the tumor cell count in histology images and the intensity of MR images. Thereafter, this information can be used as an initial condition for the tumor in the model. Machine Learning models can also be used to achieve this goal.

To increase the realism of the model, it is necessary to incorporate the mass effect, where an advection term $\nabla \cdot \big(u(x,t)v\big)$ can be added, where v is the velocity of the tumor. The mass effect is the deformation of the brain tissue caused by the growing tumor [7]. This velocity is determined by another equation, creating a coupled system [8]. The existing simulated tumor in this thesis does not consider the mechanical properties of the surrounding tissue. Incorporating the mass effect would address this limitation and bring the model closer to real-world conditions.

The simulations are run on patients with tumors that do not have an irregular shape. The tumor is planted on the healthy half part of the brain, which can cause the JI to drop, since in reality the brain is not symmetrical and no anisotropy is taken into account. This is probably the reason why the JIs in Table 5.8 have a mean 0.4592 and standard deviation of 0.0233. The selected patients also have tumors that are big enough to not distort the surrounding tissue too much. A future work would then be to test this on other patients with more irregular tumor shapes and incorporate anisotropy.

Chapter 7

Conclusion

The results of this thesis showed an improvement in performance based on the JI, with the highest JI achieved when using a combination of the gradient diffusion and a specific parameter value ($p = 1.8$) on T_1-w images. These findings show that proposed modifications can improve the simulation outcomes. Incorporating a spatially varying proliferation rate reduced the number of iterations required to reach the maximum JI compared to a constant proliferation rate.

Regarding the time aspect and realistic tumor growth, the heat maps generated by the modified model showed lower tumor cell density compared to the original model. However, the overall shape and appearance of the tumor remained similar in both models. Finally, the possibility for constructing an initial tumor cell density using H&E histology images is demonstrated.

7.1 Research Question 1

How to improve the mathematical model by optimizing its parameter.

To improve the model, the gradient diffusion is defined (3.16), a spatially varying ρ is incorporated into the model and p-Laplace is introduced into the mathematical model.

Tables 5.1–5.7 show an improvement in performance based on the JI index. Notably, the highest JI index is achieved on the T_1-w images when a combination of the gradient diffusion matrix and $p = 1.8$ is used. These findings provide insights into the potential efficacy of the proposed modifications to the standard reaction-diffusion model. By incorporating the convex diffusion matrix and p-Laplace operator. The first rows of Figures 5.3 and 5.4 illustrate subtle differences in the tumor's shape. This observation suggests that the p-Laplace operator influences the direction in which the tumor grows. Although this aspect may not be explicitly highlighted in the results Section, it is demonstrated in the experiments conducted in Section 3.5. By examining Figures 3.2–3.4, it becomes clear that when $p = 1.8$ for $T = 60$, the tumor exhibits a reduced cell density and increased size compared to the case when $p = 2$.

7.2 Research Question 2

Is it possible to extract a tumor density from patient images?

A "proof of concept" is provided showcasing the possibility of constructing an initial tumor cell density using H&E stained histology images. This constructed tumor cell density can then be used as an initial condition for the reaction-diffusion model modelling tumor growth in the brain. Unfortunately, only three slices of one block are used, which makes the initial condition construction less accurate.

7.3 Research Question 3

How can properties (such as intensity) of various MR sequences be incorporated into the model?

By defining the diffusion matrix as (3.16), the intensity of MR images such as T_1 and T_2 as well as ADC values are incorporated into the reaction-diffusion model to account for gradient diffusion. However, there is potential for further incorporation of the MR-image properties in this model.

7.4 Research Question 4

How can the simulations be evaluated? Is the tumor growth realistic?

In Tables 5.1–5.7, the simulated tumor gets a higher JI when combining the gradient diffusion, $p = 1.8$, and spatially varying ρ. However, this does not say if the growth or shape of the simulated tumor is realistic, since unrealistic tumor shapes can still get a high Jaccard index. Also, based on the Figures 5.1–5.4 alone, it is not possible to determine whether the modified reaction-diffusion model yields a more realistic tumor growth.

Bibliography

[1] Spyridon Bakas et al. *Multi-parametric magnetic resonance imaging (mpMRI) scans for de novo Glioblastoma (GBM) patients from the University of Pennsylvania Health System (UPENN-GBM) (Version 2) [Data set]*. 2021.

[2] Spyridon Bakas et al. "The University of Pennsylvania glioblastoma (UPenn-GBM) cohort: Advanced MRI, clinical, genomics, & radiomics". In: *Scientific data* 9.1 (2022), p. 453.

[3] Peter Bankhead et al. "QuPath: Open source software for digital pathology image analysis". In: *Scientific Reports* 7.1 (Dec. 2017).

[4] Allen Institute for Brain Science. *Ivy Glioblastoma Atlas Project*. Accessed [2023-03-29]. URL: http://glioblastoma.alleninstitute.org/ish.

[5] Kenneth Clark et al. "The Cancer Imaging Archive (TCIA): Maintaining and Operating a Public Information Repository". In: *Journal of Digital Imaging* 26.6 (Dec. 2013), pp. 1045–1057.

[6] Stephen J. Dalrymple et al. "Changes in proliferating cell nuclear antigen expression in glioblastoma multiforme cells along a stereotactic biopsy trajectory." In: *Neurosurgery* 35.6 (1994), pp. 1036–44.

[7] Peter Friedl et al. "Classifying collective cancer cell invasion". In: *Nature cell biology* 14.8 (2012), pp. 777–783.

[8] Luigi Graziano and Luigi Preziosi. "Mechanics in tumor growth". In: *Modeling of biological materials* (2007), pp. 263–321.

[9] Joseph P. Hornak. *The basics of MRI*. Rochester Institute of Technology, 2006. URL: http://www.cis.rit.edu/htbooks/mri.

[10] Rym Jaroudi et al. "Numerical simulations in 3-dimensions of reaction–diffusion models for brain tumour growth". In: *International Journal of Computer Mathematics* 97.6 (2020), pp. 1151–1169.

[11] Saâd Jbabdi et al. "Simulation of anisotropic growth of low-grade gliomas using diffusion tensor imaging". In: *Magnetic Resonance in Medicine: An Official Journal of the International Society for Magnetic Resonance in Medicine* 54.3 (2005), pp. 616–624.

[12] Mark Jenkinson et al. "Fsl". In: *Neuroimage* 62.2 (2012), pp. 782–790.

[13] Ender Konukoglu et al. "Image guided personalization of reaction-diffusion type tumor growth models using modified anisotropic eikonal equations". In: *IEEE transactions on medical imaging* 29.1 (2009), pp. 77–95.

[14] Denis L. Bihan et al. "Diffusion tensor imaging: concepts and applications". In: *Journal of Magnetic Resonance Imaging: An Official Journal of the International Society for Magnetic Resonance in Medicine* 13.4 (2001), pp. 534–546.

[15] Julia Larsson. "Solving the fisher equation to capture tumour behaviour for patients with low grade glioma". In: *Master's thesis Chalmers University of Technology, Gothenburg, Sweden* (2019).

[16] Gary M. Lieberman. *Second Order Parabolic Differential Equations*. World Scientific, 1996.

[17] James D. Murray. *Mathematical biology II: spatial models and biomedical applications*. Vol. 3. Springer New York, 2001.

[18] James D. Murray. *Mathematical biology: I. An introduction*. Springer, 2002.

[19] *Radiopaedia.org*. https://www.radiopaedia.org/. Accessed: 2023-05-27.

[20] Anne L. Stensjøen et al. "Growth dynamics of untreated glioblastomas in vivo". In: *Neuro-Oncology* 17.10 (Mar. 2015), pp. 1402–1411. ISSN: 1522-8517.

[21] Amanda Swan et al. "A patient-specific anisotropic diffusion model for brain tumour spread". In: *Bulletin of mathematical biology* 80 (2018), pp. 1259–1291.

[22] Kristin R. Swanson, Ellsworth C. Alvord Jr., and James D. Murray. "A quantitative model for differential motility of gliomas in grey and white matter". In: *Cell proliferation* 33.5 (2000), pp. 317–329.

[23] Kristin R. Swanson, Robert C. Rostomily, and Ellsworth C. Alvord Jr. "A mathematical modelling tool for predicting survival of individual patients following resection of glioblastoma: a proof of principle". In: *British journal of cancer* 98.1 (2008), pp. 113–119.

[24] Kristin R. Swanson et al. "Virtual and real brain tumors: using mathematical modeling to quantify glioma growth and invasion". In: *Journal of the Neurological Sciences* 216.1 (2003), pp. 1–10. ISSN: 0022-510X.

[25] Gerard J. Tortora and Bryan H. Derrickson. *Principles of Anatomy and Physiology*. 15th ed. John Wiley & Sons, 2018.

[26] Robert A. Weinberg. *The Biology of Cancer*. 2nd ed. Taylor & Francis, 2013.

[27] Yanying Zhang, Peter X. Liu, and Wenguo Hou. "Modeling of glioma growth using modified reaction-diffusion equation on brain MR images". In: *Computer Methods and Programs in Biomedicine* 227 (2022), pp. 107–233.

[28]   Yongyue Zhang, Michael Brady, and Stephen Smith. "Segmentation of brain MR images through a hidden Markov random field model and the expectation-maximization algorithm". In: *IEEE transactions on medical imaging* 20.1 (2001), pp. 45–57.